Effect of density fluctuations on lower hybrid resonance cone propagation

P. M. Bellan[a] and K. L. Wong

Plasma Physics Laboratory, Princeton University, Princeton, New Jersey 08540
(Received 21 April 1977)

Experimental measurements show that coherent, azimuthal density fluctuations (1) focus lower hybrid resonance cones azimuthally, and (2) modulate the radial location of the resonance cones. A simple theory based on wave refraction is presented; this theory is in good agreement with the experimental observations. The theory is extended to give a physical description of wave propagation through turbulent, isotropic (perpendicular to **B**) noise such as has been observed in tokamaks; it is found that the turbulence causes the lower hybrid wave vectors to have an angular spread in the plane perpendicular to **B**.

I. INTRODUCTION

At the present time the resonance cone[1,2] trajectories of externally excited lower hybrid waves have been observed in small, linear cw plasma devices,[3-6] but not in tokamaks, although attempts have been made in the case of the latter.[7] Besides differing geometrically from the linear devices, the tokamaks have different low frequency noise; for tokamaks the noise has a broad isotropic k spectrum (perpendicular to the confining field **B**) and this noise is not spatially localized,[7] whereas for the linear devices the noise is azimuthal, fairly coherent, and localized in the density gradient.

Here we present experimental results (obtained on a linear cw device) demonstrating the mechanisms by which low frequency density fluctuations affect lower hybrid waves. Further, we present a theory for these mechanisms and finally, we give some estimates of the consequences of these same mechanisms for turbulence such as is encountered in tokamaks. Our main results are: (1) coherent azimuthal noise can azimuthally focus (or filament) the lower hybrid waves and (2) turbulence spreads (in the plane $\perp$ to **B**) the directions of the **k**'s imposed by a slow-wave structure.

This paper is organized as follows: Typical experimental results obtained in the linear cw plasma are presented in Sec. II. Section III describes a theory for the propagation of resonance cones through coherent low frequency density fluctuations. Section IV contains an approximate ray tracing description which is compared with the experimental measurements of Sec. II. The effect of turbulence on lower hybrid waves is estimated in Sec. V. Finally, in Sec. VI conclusions are presented.

II. EXPERIMENT

Figure 1 shows the experimental geometry. A single ring[4] excited lower hybrid resonance cones in the L3 plasma ($n \approx 10^{10}$ cm^{-3}, $B \approx 1-2$ kG, $T_e \approx 2-5$ eV, $T_i \lesssim 0.1$ eV, He gas, plasma diameter ≈ 10 cm). The cone amplitude was small so that the drift-wave spectrum was not perturbed.[8] The radial electric field of the resonance cone was measured by a double probe (axially and radially translatable). Naturally occurring drift waves (plasma parameters were adjusted for maximum coherence of the drift waves) were picked up by a second, stationary probe, axially separated from the ring by approximately 60 cm, and radially located in the density gradient where the drift-wave amplitude was a maximum.

Since the drift-wave frequency was three orders of magnitude lower than the lower hybrid wave the drift wave behaved as a nearly static perturbation for the lower hybrid waves. The dependence of the lower hybrid wave resonance cone profile on the drift-wave phase was measured using the circuit shown in Fig. 2. Here, the drift-wave signal triggered a Princeton Applied Research 162 boxcar integrator while the resonance cone signal, after being detected (by a Hewlett-Packard 8554 spectrum analyzer in zero-scan mode, 300 kHz bandwidth), went to the boxcar input. Thus, varying the boxcar delay time would give the resonance cone profile at different phases of the drift wave. An external ramp swept both the boxcar delay time and the horizontal axis of a storage oscilloscope (vertical axis giving probe radial position). The boxcar output was algebraically added to the oscilloscope horizontal deflection, and the oscilloscope cathode ray tube cathode was pulse-modulated so as to write at discrete time intervals. When the probe moved radially through the plasma, this system gave a set of traces showing the resonance

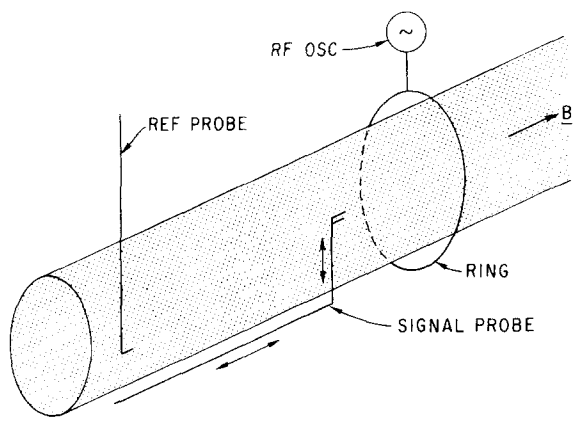

FIG. 1. Experimental setup.

[a] Present address: California Institute of Technology, Pasadena, Calif. 91125.

 0031-9171/78/2104-0592$00.90

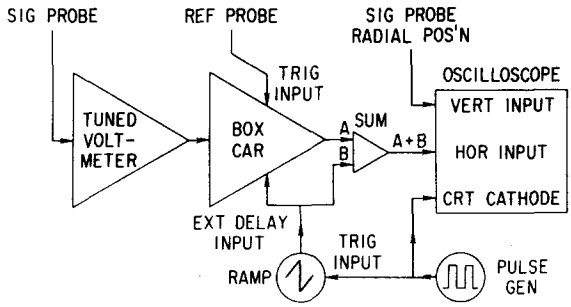

FIG. 2. Experimental electronics—block diagram.

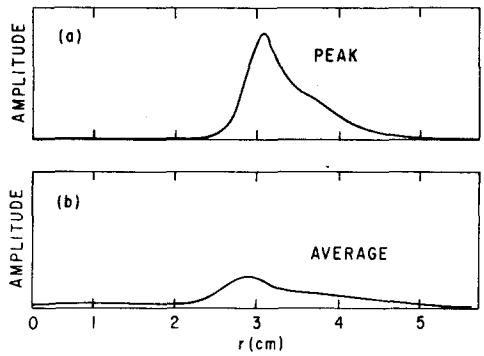

FIG. 4. Peak resonance cone amplitude compared to average.

cone field at a sequence of delay times relative to the drift wave phase. Figure 3(a) shows typical data (photos are rotated 90°) obtained this way (here, the lower hybrid wave is at 70 MHz and the time separation between vertical traces on the photos is 4.1 μsec). Figure 3(b) shows the drift-wave phase at the same sequence of delay times (this was obtained from one tip, biased for ion saturation current, of the double probe).

Two phenomena are apparent in Fig. 3: (1) the radial position of the resonance cone oscillates, moving outward when the drift-wave fluctuation is positive, and (2) when the resonance cone moves out, its amplitude increases greatly. In fact, Fig. 4 shows that the peak amplitude can be over three times the average amplitude (the latter measured by free-running the boxcar trigger), thus the energy density at the peak is about an order of magnitude greater than the average energy density. This behavior constitutes an azimuthal focusing of the resonance cone by the drift wave. Because the drift waves are rotating azimuthally, the focusing of the resonance cones is similarly rotating, and since the drift wave varies as $\cos(m\theta - \omega_d t)$, the vertical axis of Fig. 3(a) can also be considered the azimuthal coordinate. As shown in Fig. 5, the focusing ratio (peak amplitude: average amplitude) increases as the lower hybrid wave penetrates into the plasma (the measurements here were made at successive axial probe positions).

In Fig. 6 both the focusing and the trajectory modulation are seen to increase as the resonance cone penetrates the plasma (increasing z, decreasing r). For Fig. 6 the boxcar output was used to intensity modulate an oscilloscope; the horizontal axis corresponds to radial position, the vertical to the boxcar delay [200 μsec compared with 50 μsec for Fig. 3(a)].

k, the azimuthal wavenumber of the drift wave (an important quantity for the theory of the next section), may be deduced from Fig. 7(a) which was obtained from interferometry with an azimuthal probe. Due to azimuthal asymmetry of the plasma k is not constant; for the azimuth of the double probe [arrow in Fig. 7(a)] $k \approx 2.2\ \text{cm}^{-1}$. Figures 7(b) and 8 are used as guides for the numerical ray tracing presented in Sec. IV. Figure 7(b) shows contours of constant drift-wave amplitude measured with a simple contour plotting circuit (the horizontal axis is the probe position, the vertical axis is the boxcar delay time). The vertical "droplets" correspond to alternating signs of the drift wave. Figure 8 shows the density profile and the drift-wave amplitude profile. The drift wave strength $\epsilon \equiv \delta n/n$ is ≈ 0.3. Finally, Fig. 9 shows that the lower hybrid wave spectrum typically has many sidebands at harmonics of the drift

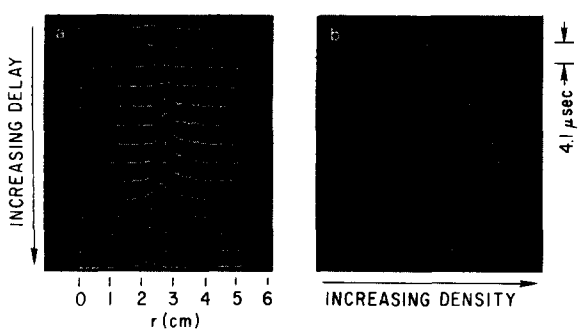

FIG. 3. (a) Typical experimental data showing resonance cone position being modulated and resonance cone amplitude increasing when moving out. (b) Drift-wave phase corresponding to (a).

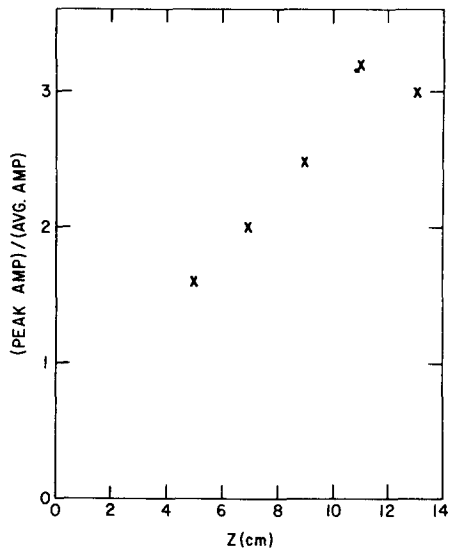

FIG. 5. Strength of focusing (ratio of peak to average amplitude) vs axial position.

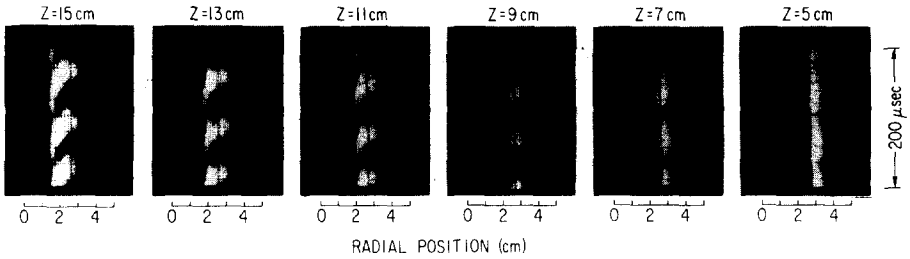

FIG. 6. Intensity modulation showing trajectory modulation and focusing when probe is at a sequence of axial positions.

wave frequency, ω_d. The shape of this spectrum varies with the radial position of the probe. The oscillation of the resonance cone through the probe position produces an apparent pulse modulation of the rf; such a modulation gives comb-like spectra such as shown in Fig. 9.

From this experimental data it is clear the drift waves are azimuthally focusing the resonance cones and also causing them to oscillate radially. This modification of the resonance cones is rotating at the azimuthal phase velocity of the drift waves. Let us now derive a simple theory which will explain these observations.

III. RESONANCE CONE PROPAGATION THROUGH A COHERENT AZIMUTHAL DRIFT WAVE

We now examine the propagation in slab geometry ($\hat{z} \parallel \mathbf{B}$; $x \parallel \nabla n$; y corresponds to azimuthal direction of cylindrical geometry) of a lower hybrid wave through a radially localized, coherent, azimuthal drift wave,

$$n_d(\mathbf{x}, t) = \epsilon g(x) n(x) \cos(ky - \omega_d t) , \tag{1}$$

where $\epsilon \equiv \max(n_d)/n(x)$ is the normalized drift-wave strength, $g(x)$ is the drift-wave profile, k and ω_d are the respective wavenumber and frequency of the drift wave. The density profile is taken as $h(x)$ so that $n(x) = h(x) n_0$, where n_0 is the density at the center. We assume that $\epsilon \ll 1$, that $g(x)$ assumes its maximum value, unity, at $x = a$ and has a width Δ about $x = a$, where a is located in the gradient of $h(x)$.

The lower hybrid wave frequency, ω, greatly exceeds the drift frequency, ω_d, so that we may retain the explicit drift-wave time dependence in the lower hybrid wave equation, and treat this dependence as a slowly varying parameter. By assuming that the lower hybrid wave does not modify the drift wave (experimental investigations of modifications of the drift-wave spectrum by large amplitude lower hybrid waves have also been carried out[8]) the following equation is found to govern lower hybrid wave propagation in the presence of drift waves:

$$\frac{\partial}{\partial x} K_\perp \frac{\partial \phi}{\partial x} + \frac{\partial}{\partial y} K_\perp \frac{\partial \phi}{\partial y} + \left[1 - \frac{\omega_{pe}^2}{\omega^2}\left(1 + \frac{n_d(x,t)}{n(x)}\right)\right] \frac{\partial^2 \phi}{\partial z^2} + \frac{i\omega_{pe}^2}{\omega \omega_{ce}} \nabla\left(\frac{n_d(x,t)}{n(x)}\right) \cdot \nabla\phi \times \hat{z} = 0 . \tag{2}$$

Here, ω_{pe} and ω_{ce} are the respective electron plasma and cyclotron frequencies, $K_\perp = 1 - \omega_{pi}^2/\omega^2 + \omega_{pe}^2/\omega_{ce}^2$, where ω_{pi} is the ion plasma frequency, and ϕ is the lower hybrid wave potential. Drift-wave modifications to $K_\perp$ have been dropped because $\omega_{pi}^2/\omega^2 \ll 1$ and $\omega_{pe}^2/\omega_{ce}^2 \ll 1$ at locations where $g(x)$ is finite. The last term in Eq. (2) comes from $\mathbf{E} \times \mathbf{B}$ coupling. Defining

$$\zeta \equiv \omega z/\omega_{pe_0} ,$$
$$q(\mathbf{x}, t) \equiv 1 + n_d(\mathbf{x}, t)/n(x) = 1 + \epsilon g(x) \cos(ky - \omega_d t) , \tag{3}$$
$$\Lambda(\mathbf{x}, t) \equiv i(\omega_{pe_0}^2/\omega\omega_{ce}) k g(x) h(x) \sin(ky - \omega_d t)$$

(where ω_{pe_0} is the electron plasma frequency at the center), Eq. (2) becomes

$$\frac{\partial}{\partial x} K_\perp \frac{\partial \phi}{\partial x} + \frac{\partial}{\partial y} K_\perp \frac{\partial \phi}{\partial y} - h(x) q(\mathbf{x}, t) \frac{\partial^2 \phi}{\partial \zeta^2} + \epsilon \Lambda(\mathbf{x}, t) \frac{\partial \phi}{\partial x} = 0 . \tag{4}$$

One is tempted to solve Eq. (4) by expanding $\phi = \phi_0 + \epsilon\phi_1 + \cdots$ (where $|\epsilon\phi_1| \ll |\phi_0| \ldots$) and then solving for ϕ_1 in terms of ϕ_0. This scheme will not work here, be-

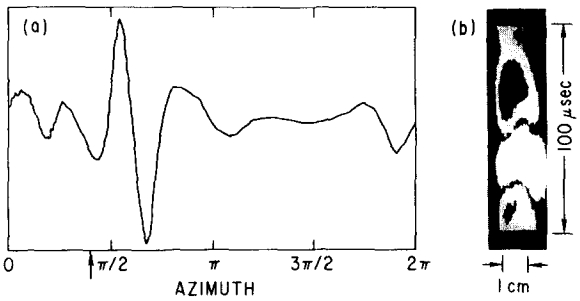

FIG. 7. (a) Azimuthal probe interferometer signal. Arrow shows azimuths of double probe used in Figs. 3–6. (b) Contours of constant drift-wave amplitude; vertical droplet-shapes correspond to alternating sign of drift wave.

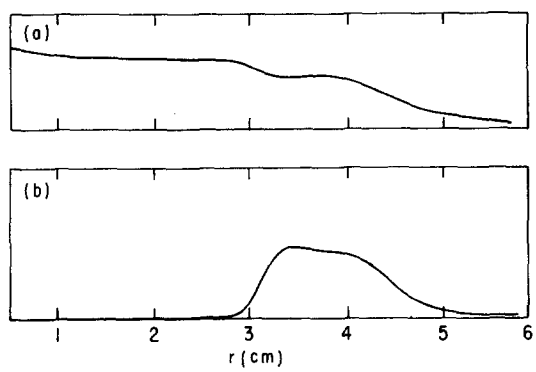

FIG. 8. (a) Density profile; (b) drift-wave amplitude profile.

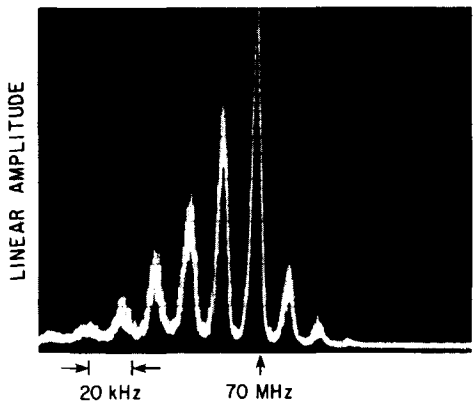

FIG. 9. Frequency spectrum of lower hybrid wave.

cause the resonance cone trajectory, being modulated [by virtue of the coefficient $q(\mathbf{x}, t)$ of $\partial^2\phi/\partial\zeta^2$] can shift its location to places where $\phi_0 = 0$; at these places $|\epsilon\phi_1| \gg |\phi_0|$. Thus, a method incorporating trajectory modulation is required. The Eikonal method (effectively geometrical optics) turns out to be suitable, since the cones are sharper than the scale length of the density inhomogeneity. We will now describe an analytic solution of Eq. (4); a ray tracing solution will be discussed in Sec. IV.

For $\epsilon = 0$, and a source uniform in y, Eq. (4) has the well-known solution $\phi = A(x)\Phi[\zeta - f(x)]\exp(-i\omega t)$, where $A(x)$ is a WKB "swelling factor" and $f(x)$ gives the resonance cone trajectory. For $\epsilon \neq 0$, we might reasonably assume the y dependence of ϕ to be

$$\phi(\mathbf{x}) = A(x, y)\Phi[\zeta - f(x, y)]\exp(-i\omega t) \ . \tag{5}$$

The trajectories are now the curves $\zeta = f(x, y)$. It should be noted that Eq. (5) breaks down if several trajectories in the $x - y$ plane cross each other (this point will be discussed in Sec. IV).

Substituting Eq. (5) into Eq. (4) and, in the spirit of the Eikonal method, insisting first that the coefficient of ϕ'' be zero, then that the coefficient of Φ' be zero, we find

$$f_x^2 + f_y^2 = [h(x)/K_\perp(x)][1 + \epsilon g(x)\cos(ky - \omega_d t)] \ , \tag{6a}$$

and

$$\left(f_x \frac{\partial}{\partial x} + f_y \frac{\partial}{\partial y}\right) \ln A^2 = -\left(f_{xx} + f_{yy} + f_x \frac{\partial \ln K_\perp}{\partial x} + \epsilon\Lambda f_x\right) . \tag{6b}$$

A solution to Eq. (6a), correct to first order in ϵ, gives the trajectory as

$$f(x, y) = \int_0^x [h(x')/K_\perp(x')]^{1/2} \times [1 + \epsilon g(x')\cos(ky - \omega_d t)]^{1/2}\, dx' \ ; \tag{7}$$

this may be used to give the various f derivatives in Eq. (6b). Noting that $f_x \sim O(1)$, whereas f_y, $f_{yy} \approx O(\epsilon)$, we drop $f_y\partial/\partial y$ with respect to $f_x\partial/\partial x$ in Eq. (6b) and integrate, obtaining

$$A = A_s A_e A_r \ , \tag{8}$$

where

$$A_s = [h(x)K_\perp(x)]^{-1/4}[1 + \epsilon g(x)\cos(ky - \omega_d t)]^{-1/4} \ , \tag{9a}$$

$$A_e = \exp\left[-\tfrac{1}{2} i\epsilon(\omega_{pe0}^2/\omega\omega_{ce})k\sin(ky - \omega_d t) \times \int_0^x g(x')h(x')dx'\right] \ , \tag{9b}$$

and

$$A_r = 1 + \tfrac{1}{4} k^2\epsilon\cos(ky - \omega_d t)\int_0^x dx'[K_\perp(x')/h(x')]^{1/2} \times \int_0^{x'} dx'' h^{1/2}(x'')g(x'') \ . \tag{9c}$$

The respective physical interpretations for f, A_s, A_e, and A_r are the following: f gives the resonance cone trajectory $\zeta = f(x, y)$; Eq. (7) show that the drift waves modulate the trajectory causing the resonance cone to be pushed outward when the density fluctuation is positive (in agreement with the experiment, cf. Fig. 3). The WKB "swelling factor," A_s, gives a small amplitude modulation, but only at the drift wave [i.e., where $g(x)$ is finite]. The $\mathbf{E} \times \mathbf{B}$ factor, A_e, comes from the last term in Eq. (2) and represents a phase modulation. Because this modulation contains an integral over $g(x)$, it builds up to some constant value as the lower hybrid wave passes through the drift-wave layer. Since $|A_e| = 1$, this factor does not affect the overall amplitude; closer analysis shows that it rather desymmetrizes the relative amplitudes of the drift-wave-induced sidebands of the lower hybrid wave. The last factor, A_r, comes from a refractive, azimuthal focusing of the resonance cone. A_r builds up as the lower hybrid wave passes through the drift wave, and *continues to increase* even after the lower hybrid wave has passed through the drift wave; this is evident from the double integral in Eq. (9c). A physical picture is that the drift waves are acting like an azimuthally periodic, rotating system of lenses which focus the resonance cone. In agreement with the experimental results shown in Fig. 3, the focusing is at a maximum when $\cos(ky - \omega_d t) = 1$. Consideration of $f_x\partial A_r/\partial x : f_y\partial A_r/\partial y$ shows that the dropping of $f_y\partial/\partial y$ is valid [and hence Eq. (9c) is valid] only when $k^2\epsilon(x - a)\Delta/2 \ll 1$, i.e., when the focusing is weak.

IV. RAY TRACING SOLUTION OF EQUATION (4)

The analytic description of Sec. III gave the main physical mechanisms but broke down when the focusing became strong. Let us now solve Eq. (4) using ray tracing to determine what happens beyond the validity of the analytic solution.

Now, we consider $f(x, y)$ as the trajectory of a *single* ray in the $x - y$ plane and so implicitly allow rays to cross. Equation (6a) becomes a local condition which the ray trajectory must continually satisfy, i.e., along the ray trajectory,

$$\delta D(f_x, f_y, x, y) = 0 \ , \tag{10}$$

where $D \equiv f_x^2 + f_y^2 - [h(x)/K_\perp(x)][1 + \epsilon g(x)\cos(ky - \omega_d t)]$. Introducing the path parameter τ, Eq. (10) becomes

$$\delta D=\left(\frac{\partial D}{\partial f_x}\frac{df_x}{d\tau}+\frac{\partial D}{\partial x}\frac{dx}{d\tau}+\frac{\partial D}{\partial f_y}\frac{df_y}{d\tau}+\frac{\partial D}{\partial y}\frac{dy}{d\tau}\right)d\tau=0\,, \qquad (11)$$

which may be satisfied for arbitrary $d\tau$ if

$$\frac{dx}{d\tau}=\frac{\partial D}{\partial f_x} \qquad \frac{dy}{d\tau}=\frac{\partial D}{\partial f_y}\,, \qquad (12a)$$

$$\frac{df_x}{d\tau}=-\frac{\partial D}{\partial x} \qquad \frac{df_y}{d\tau}=-\frac{\partial D}{\partial y}\,. \qquad (12b)$$

Combining Eqs. (12) gives

$$\frac{d^2x}{d\tau^2}=2\,\frac{\partial}{\partial x}\left\{\left[\frac{h(x)}{K_\perp(x)}\right]\left[1+\epsilon g(x)\cos(ky-\omega_d t)\right]\right\},$$

$$\frac{d^2y}{d\tau^2}=2\,\frac{\partial}{\partial y}\left\{\left[\frac{h(x)}{K_\perp(x)}\right]\left[1+\epsilon g(x)\cos(ky-\omega_d t)\right]\right\}. \qquad (13)$$

Equations (13) give the ray trajectories $x(\tau)$, $y(\tau)$; in general, these equations must be solved numerically. From Eqs. (12a) the appropriate boundary conditions at $\tau=0$ are $dx/d\tau=2f_x|_{\tau=0}$, $dy/d\tau=2f_y|_{\tau=0}$; from Eq. (7) these become $dx/d\tau=2\{h[x(0)]\}^{1/2}$, and $dy/d\tau=0$ at $\tau=0$. These boundary conditions insure that all rays, irrespective of their initial y, have the trajectory $\zeta=\int_0^x h^{1/2}(x)\,dx$, before they encounter the drift wave. To find $f(x,y)$ on a particular ray we note that $df=(f_x\,dx/d\tau+f_y dy/d\tau)d\tau=2(f_x^2+f_y^2)d\tau$ so that

$$f[x(\tau),y(\tau)]=2\int_0^\tau\left(\{h[x(\tau')]/K_\perp[x(\tau')]\}\times\{1+\epsilon g[x(\tau')]\cos[ky(\tau')-\omega_d t]\}\right)d\tau'\,. \qquad (14)$$

Thus, to find $f(x,y)$ at a particular point on a particular ray, we must first use Eqs. (13) to obtain the ray trajectories $x(\tau)$, $y(\tau)$, and then use Eq. (14).

$x(\tau)$, $y(\tau)$, and f were computed numerically from Eqs. (13) and (14), for plasma parameters similar to those of the experiment described in Sec. II. In particular, the computation used $\epsilon=0.3$, $K_\perp=1$, $h(x)=\tanh(x/L)$ where $L=1.5$ cm, $g(x)=\exp[-(x-a)^2/\Delta^2]$ where $a=1.6$ cm and $\Delta=0.8$ cm, and $k=2.16$ cm^{-1}. Figure 10(a) shows $h(x)$ and $g(x)$ while Fig. 10(b) gives the calculated ray trajectories $x(\tau)$, $y(\tau)$ for various initial values of y. The concentric ellipses in Fig. 10(b) are contours of constant drift-wave amplitude, analogous to those of Fig. 7(b). The dashed lines are the surfaces of constant z, i.e., surfaces of constant f obtained from Eq. (14).

The dashed lines in Fig. 10(b) can also be interpreted to be the phase fronts of waves generated by a slow-wave structure. This is so because the different z surfaces of Fig. 10(b) refer to the axial *displacement* from the transmitting element to the observation point. Thus, instead of having one transmitting point and a sequence of observation points (the interpretation until now), one could rather have one fixed observation point and a sequence of transmitting points at different z's (i.e., a slow-wave structure). This interpretation holds providing that rays emanating from different slow-wave structure elements all see the same density fluctuation; this is so for the usual case where the axial wavelength of the density fluctuation greatly exceeds that of the slow-wave structure.

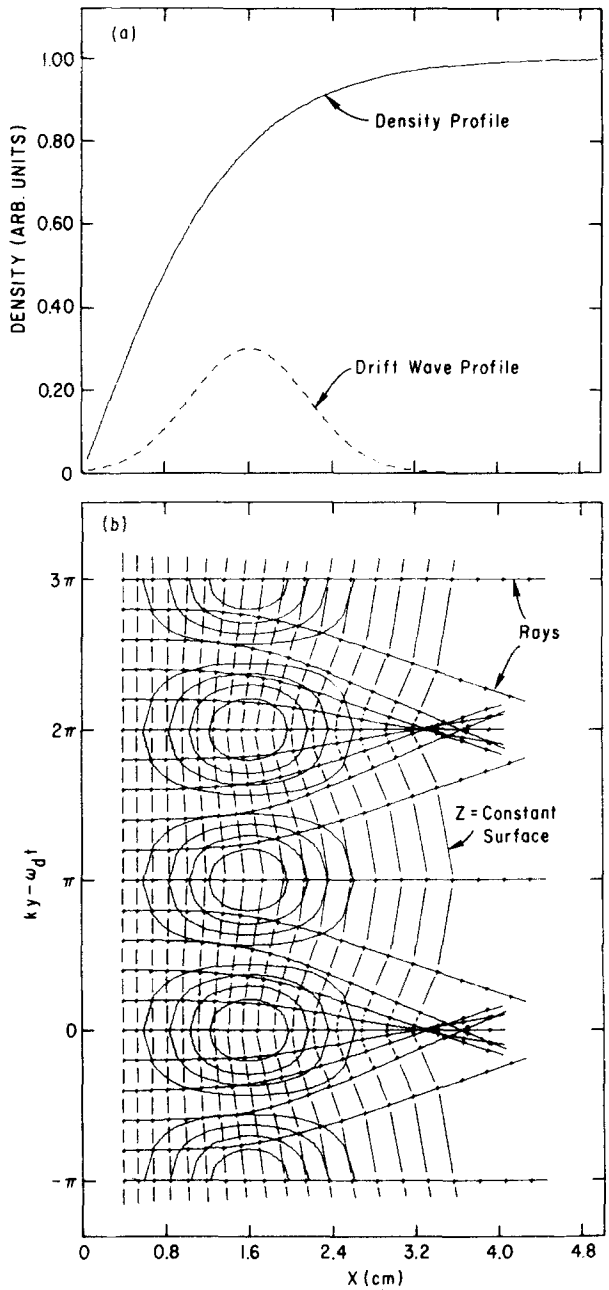

FIG. 10. (a) Density and drift-wave profiles used for numerical integration of Eqs. (13) and (14). (b) Ray refraction in the x-y plane. Concentric ellipses are constant drift-wave amplitude contours.

Figure 10 also shows how the ray refraction depends on the initial location of the ray on the y axis. Rays for which initially $\cos(ky-\omega_d t)=\pm1$ are not deflected in y; other rays are deflected. Examination of the constant z surfaces shows that focusing occurs when the resonance cone trajectory has been pushed radially outward [i.e., when $\cos(ky-\omega_d t)=+1$]. This is in agreement with the experimental observations presented in Fig. 3.

The ray convergence is related to the A_r factor of Sec. II as follows: At $x\approx a$ the ray trajectory is hardly changed so that here Eq. (7) gives f adequately. Thus for $x\gtrsim a$, $f_x\approx[h(x)/K_\perp(x)]^{1/2}$ and $f_y\approx-\frac{1}{2}k\Delta\epsilon h^{1/2}(a)$

$\times \sin[ky(a) - \omega_d t]$, where $y(a)$ is the value of y at $x = a$. From Eqs. (12a)

$$dy/dx = f_y/f_x \; ; \tag{15}$$

this may be integrated from $x = a$ giving

$$y \approx y(a) - \tfrac{1}{2} k\Delta\epsilon h^{1/2}(a) \sin[ky(a) - \omega_d t] \times \int_a^x dx' [K_\perp(x')/h(x')]^{1/2} , \tag{16}$$

a good approximation to the rays shown in Fig. 10(b). In Eq. (16) $y(a)$ depends on y transcendentally, and in fact, there may be several $y(a)$'s for a particular y. This nonuniqueness comes from ray crossing and explains why the analytic solution broke down. However, before there is crossing, the relation is one-to-one so that the analytic solution is valid. The ray concentration, i.e., the energy focusing, is then inversely proportional to the separation between adjacent rays, i.e., proportional to $dy(a)/dy$. From Eq. (16) we find

$$\phi \sim \left(\frac{dy(a)}{dy}\right)^{1/2} = 1 + \tfrac{1}{4} k^2 \epsilon\Delta h^{1/2}(a) \cos[ky(a) - \omega_d t] \times \int_a^x dx' [K_\perp(x')/h(x')]^{1/2} \tag{17}$$

which corresponds approximately to Eq. (9c). Here, $y(a)$ replaces the y of Eq. (9c), thus when $y \approx y(a)$ (i.e., when there is small deflection), Eq. (9c) should be correct.

V. RAY BEHAVIOR IN TURBULENT PLASMAS

In tokamak plasmas the low frequency density fluctuations have been observed to be turbulent and nonlocalized and also to have an isotropic (perpendicular to B) k spectrum[7]; hence, the coherent focusing and trajectory modulation discussed in Secs. II–IV cannot be expected. Let us now use the ray tracing method of Sec. IV to determine lower hybrid wave behavior in turbulent, nonlocalized, isotropic density fluctuations. This will give a fairly realistic picture of what linear lower hybrid waves should look like in a tokamak plasma.

We assume that the turbulent density fluctuation k spectrum varies as $\exp[-(k_x^2 + k_y^2/\kappa^2]$, where κ is a correlation length. For simplicity, let us consider a uniform plasma $[h(x) = 1]$ with $K_\perp \approx 1$, so that Eq. (13) becomes

$$\ddot{\mathbf{x}} = -\nabla\Psi(\mathbf{x}) , \tag{18}$$

where $\Psi(\mathbf{x}) = -2n_d(\mathbf{x})/n_0$, $\mathbf{x} = (x, y)$, a dot means $d/d\tau$, and we have suppressed the slow time variation of n_d. The associated boundary conditions are $\dot{\mathbf{x}}|_{\tau=0} \equiv v_0 = 2$ and $\dot{y}|_{\tau=0} = 0$ so that all the rays are initially given by $\zeta = x$. Equation (18), which is formally similar to the motion of a particle in a turbulent field, can be solved approximately by substituting the orbits $x = x_0 + v_0\tau + \delta x$, $y = y_0 + \delta y$ into the right-hand side. If $k\delta x \ll 2\pi$ and $k\delta y \ll 2\pi$ for the largest k's of the turbulence [which are $\Theta(\kappa)$], then we may drop δx and δy and use only the zero-order orbits $x = x_0 + v_0\tau$, $y = y_0$ on the right-hand side of Eq. (18). Doing this, integrating twice, and using the boundary conditions $\delta\dot{x} = \delta\dot{y} = \delta x = \delta y = 0$ at $\tau = 0$ we obtain

$$\delta x = \int_{-\infty}^{\infty} dk_x \int_{-\infty}^{\infty} dk_y \{ik_x\tilde{\Psi}(k_x, k_y)[\exp(ik_x v_0\tau) - 1 - ik_x v_0\tau] \exp(ik_x x_0 + ik_y y_0)/k_x^2 v_0^2\} , \tag{19}$$

with corresponding expressions for δy, $\delta\dot{x}$, and $\delta\dot{y}$ [here, $\tilde{\Psi}(k_x, k_y)$ is the Fourier transform of $\Psi(\mathbf{x})$]. Since averaging over initial positions in a turbulent field is equivalent to averaging over an ensemble of turbulent fields, the ensemble average (denoted by a bar) of δx^2 is

$$\overline{\delta x^2} = (2L)^{-2} \int_{-L}^{L} dx_0 \int_{-L}^{L} dy_0 [\delta x(x_0, y_0)]^2 . \tag{20}$$

Similar expressions give $\overline{\delta y^2}$, $\overline{\delta\dot{x}^2}$, and $\overline{\delta\dot{y}^2}$. Substituting Eq. (19) into Eq. (20) gives

$$\overline{\delta x^2} = \frac{8\pi^2}{L^2} \int_0^{\infty} dk_x \int_0^{\infty} dk_y \{|\tilde{\Psi}(\mathbf{k})|^2 \times [1 - \cos(k_x v_0\tau) + (k_x v_0\tau)^2/2 - k_x v_0\tau \sin(k_x v_0\tau)]/k_x^2 v_0^4\} . \tag{21}$$

Since

$$\overline{\Psi^2(\mathbf{x})} = (2L)^{-2} \int_{-L}^{L} dx \int_{-L}^{L} dy \, \Psi(\mathbf{x})^2 = (2\pi/L)^2 \int_0^{\infty} dk_x \int_0^{\infty} dk_y |\tilde{\Psi}(\mathbf{k})|^2 , \tag{22}$$

the appropriately normalized spectrum is

$$|\tilde{\Psi}(\mathbf{k})|^2 = \overline{\Psi}^2 L^2 \exp(-k^2/\kappa^2)/\pi^3\kappa^2 . \tag{23}$$

Substituting Eq. (23) into Eq. (21) and performing the k_y integrals gives

$$\overline{\delta x^2} = \frac{4}{\sqrt{\pi}} \frac{\overline{\Psi}^2\tau}{\kappa v_0^3} \times \int_0^{\infty} d\eta \{\exp[-\eta^2/(\kappa v_0\tau)^2] (1 - \cos\eta + \eta^2/2 - \eta\sin\eta)/\eta^2\} . \tag{24}$$

The corresponding procedure for $\overline{\delta y^2}$, $\overline{\delta\dot{x}^2}$, and $\delta\dot{y}^2$ gives

$$\overline{\delta y^2} = \frac{2\kappa}{\sqrt{\pi}} \frac{\overline{\Psi}^2\tau^3}{v_0} \times \int_0^{\infty} d\eta \{\exp[-\eta^2/(\kappa v_0\tau)^2](1 - \cos\eta + \eta^2/2 - \eta\sin\eta)/\eta^4\} , \tag{25}$$

$$\overline{\delta\dot{x}^2} = (4\overline{\Psi}^2/\sqrt{\pi}\kappa v_0^3\tau) \int_0^{\infty} d\eta \exp[-\eta^2/(\kappa v_0\tau)^2] (1 - \cos\eta) , \tag{26}$$

$$\delta\dot{y}^2 = (2\overline{\Psi}^2\kappa\tau/\sqrt{\pi}v_0) \times \int_0^{\infty} d\eta \exp[-\eta^2/(\kappa v_0\tau)^2] (1 - \cos\eta)/\eta^2 . \tag{27}$$

For $\kappa v_0\tau \gg 1$ (i.e., the lower hybrid wave has traveled several correlation lengths of the turbulence), the integrals in Eqs. (24)–(27) may be evaluated approximately, using a technique described in the Appendix. The expressions thus obtained are

$$\overline{\delta x^2} = \overline{\Psi}^2\tau^2/v_0^2 , \tag{28a}$$

$$\overline{\delta y^2} = \sqrt{\pi}\kappa\overline{\Psi}^2\tau^3/3v_0 , \tag{28b}$$

$$\overline{\delta\dot{x}^2} = 2\overline{\Psi}^2/v_0^2 , \tag{28c}$$

and

$$\delta\dot{y}^2 = \sqrt{\pi}\kappa\overline{\Psi^2}\tau/v_0 \ . \tag{28d}$$

Finally, let us calculate $\delta\zeta$. From Eq. (14), Eq. (10), and Eq. (12a) [all with the present turbulent field replacing $\epsilon g(x)\cos(ky - \omega_d t)$],

$$\zeta + \delta\zeta = \frac{1}{2}\int_0^\tau [(v_0 + \delta\dot{x})^2 + (\delta\dot{y})^2]\, d\tau \tag{29}$$

so that

$$\delta\zeta = \int_0^\tau v_0\delta\dot{x}\, d\tau = v_0\delta x \ . \tag{30}$$

Thus, $\delta\zeta$ and δx are not independent. Since $x = v_0\tau$, $v_0 = 2$, $\overline{\Psi^2} = 4(\delta n/n)^2 = 4\epsilon^2$, $\zeta = z\omega/\omega_{pe_0}$, Eqs. (28) become

$$\overline{\delta x^2} = \epsilon^2 x^2/4 \ , \tag{31a}$$

$$\overline{\delta y^2} = \sqrt{\pi}\epsilon^2\kappa x^3/12 \ , \tag{31b}$$

$$\overline{\delta\dot{x}^2} = 2\epsilon^2 \ , \tag{31c}$$

$$\overline{\delta\dot{y}^2} = \sqrt{\pi}\epsilon^2\kappa x \ , \tag{31d}$$

and Eq. (30) becomes

$$\delta z/z = 2\delta x/x \ . \tag{32}$$

The factor 2 in Eq. (32) shows that perturbed rays do not lie on the corresponding unperturbed ray (which would have been so if the factor had been unity). Equations (31) hold when $\kappa\delta x < 2\pi$ and $\kappa\delta y < 2\pi$. From Ref. 7, for a typical tokamak plasma $\epsilon \equiv \delta n/n \approx 0.03$ and $2\pi/\kappa \approx 1$ cm, so that at $x = 10$ cm Eqs. (31) give $\delta x_{\rm rms} \approx 0.15$ cm and $\delta y_{\rm rms} \approx 0.9$ cm. From Eqs. (31c) and (31d) it can be seen that the ray directions will have a distribution of angles with half-width

$$\Delta\theta \approx \frac{\delta\dot{y}_{\rm rms}}{v_0 + \delta\dot{x}_{\rm rms}} \approx \frac{\delta\dot{y}_{\rm rms}}{v_0} = \pi^{1/4}2^{-1/2}\epsilon(\kappa x)^{1/2} \ ; \tag{33}$$

for the parameters[9] of Ref. 7, $\Delta\theta \approx 0.16$ rad at $x = 10$ cm.

In order to understand intuitively what Eqs. (31)–(33) mean, ray trajectories through a two-dimensional turbulent density fluctuation field were calculated numerically by means of the ray-tracing program used for Fig. 10(b). The turbulent field consisted of a Gaussian-weighted [as in Eq. (25)], normalized sum of sinusoidal plane waves, each with a different k_x and k_y, and each with a random phase $(0 - 2\pi)$ obtained from a random number generator. Twelve k_x's and twelve k_y's were used so that there were 144 plane waves in the sum. Figure 11(a) shows a portion of the turbulent field ($y = 5$ cm, $x = 0$ to 16 cm).

Numerically calculated ray trajectories for this turbulent situation are shown in Fig. 11(b). The small dots and squares on the rays show increments of z while the vertical slashed lines show the first few phase fronts of waves excited by a slow wave structure. The turbulence-induced x and y displacements, δx and δy, of the rays are clearly evident; as expected, $\delta y \gg \delta x$. The rays are grouped in bundles having a characteristic y dimension of order $2\pi/k$, rays within a bundle all see approximately the same turbulent field and so have approximately the same trajectory. At large x, the bundles overlap each other giving interference patterns. Also

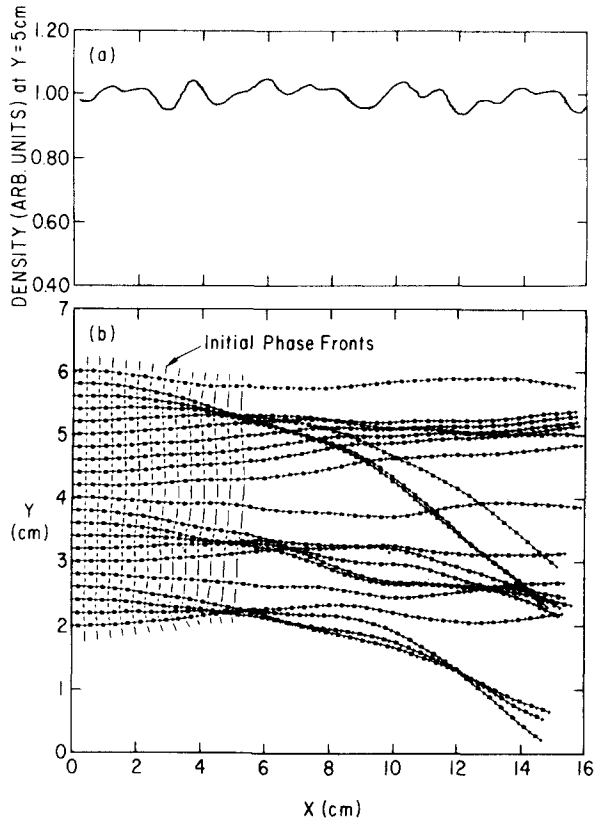

FIG. 11. (a) Turbulent density profile at $y = 5$ cm. (b) Ray trajectories. The initial phase fronts (i.e., before complicated crossing occurs) of waves generated by a slow-wave structure are shown. Turbulence randomly refracts bundles of rays. $\kappa = 2\pi$ cm^{-1}, $\epsilon = 0.03$.

at large x, the wave vectors associated with the different bundles (wave vectors point in the same direction as the ray trajectory) have a spread in direction. The angular spread is given by Eq. (33).

VI. CONCLUSIONS

We have shown the effect of low frequency density fluctuation noise on lower hybrid resonance cone propagation. In particular, this noise has been shown to refract lower hybrid resonance cones. If the noise is coherent, azimuthal, and radially localized, as is so for the experimental results presented in Sec. II, then the refraction focuses the resonance cones in the azimuthal direction and modulates their radial location. Experimental measurements show that the energy density in the focal regions can exceed the average energy density by an order of magnitude. The theory used to describe the experimental results presented here has been extended to provide what should be a fairly realistic picture of linear lower hybrid waves propagating through turbulent, nonlocalized, and isotropic (perpendicular to **B**) noise such as has been observed in tokamaks. It is found that here the lower hybrid wave vectors develop a spread in direction in the plane perpendicular to **B**, and for typical tokomak parameters[9] this spread has a half width of 0.16 rad.

ACKNOWLEDGMENTS

One of the authors (P. B.) wishes to thank Dr. P. K. Kaw, Dr. M. Porkolab, and Dr. C. Surko for useful discussions. The technical assistance of J. Johnson and J. Taylor is gratefully appreciated.

This work was supported by U. S. Energy Research and Development Administration Contract E(11-1)-3073.

APPENDIX. EVALUATION OF INTEGRALS FOR EQ. (28)

The integral for Eq. (26) is well known. The remaining integrals may be estimated by comparing the profile of the Gaussian with the profile of the other factor in the integrand, and then integrating over whichever factor has the narrower profile. For Eqs. (25) and (27) the non-Gaussian factors are finite at $\eta = 0$ and fall off as η^{-2} for $\eta \gtrsim 1$ whereas the Gaussian is approximately constant for $0 < \eta \lesssim 1$ since $\kappa v_0 \tau \gg 1$. Thus, the non-Gaussian factors are narrower; integration over these functions (with the Gaussian approximated as unity) gives Eqs. (28b) and (28d). For Eq. (24) the non-Gaussian factor has a magnitude of 0.5 except for a small region $0 < \eta \lesssim 1$; hence, the Gaussian factor is narrower here. Integration over the Gaussian gives Eq. (28a).

[1]J. Dawson and C. Oberman, Phys. Fluids **2**, 103 (1959).
[2]H. H. Kuehl, Phys. Fluids **5**, 1095 (1962).
[3]R. K. Fisher and R. W. Gould, Phys. Fluids **14**, 857 (1971).
[4]R. J. Briggs and R. R. Parker, Phys. Rev. Lett. **29**, 852 (1972).
[5]P. Bellan and M. Porkolab, Phys. Rev. Lett. **34**, 124 (1975).
[6]P. L. Colestock and W. D. Getty, in *Proceedings of the Second Topical Conference on rf Plasma Heating* (Texas Tech University, Lubbock, Tex., 1974), paper B-3.
[7]C. M. Surko and R. E. Slusher, Phys. Rev. Lett. **37**, 1747 (1976).
[8]K. L. Wong and P. M. Bellan (to be published).
[9]*Note added in proof*: Recent scattering experiments on the Alcator tokamak [R. E. Slusher and C. M. Surko, Phys. Rev. Lett. **40**, 400 (1978)] show that $\delta n/n \simeq 1$ can occur at the plasma periphery; hence a much more drastic angular spreading may be expected than for the $\delta n/n = 0.03$ case considered at the end of Sec. V [c.f., Eq. (33)]. Although the small $\epsilon (= \delta n/n)$ expansion used in our paper breaks down when $\delta n/n \simeq 1$, numerical calculations similar to Fig. 11(b) suggest that for such large $\delta n/n$ the rays may spread up to 180° from their original direction, thus reducing the accessibility of the rf to the plasma interior.